remote sensing

MDPI

Article

Multiple Characteristics of Precipitation Inferred from Wind Profiler Radar Doppler Spectra

Albert Garcia-Benadi [1,2], Joan Bech [2,3,*], Mireia Udina [2], Bernard Campistron [4] and Alexandre Paci [5]

[1] SARTI, Universitat Politècnica de Catalunya, 08800 Vilanova i la Geltrú, Spain
[2] Department of Applied Physics—Meteorology, University of Barcelona, 08028 Barcelona, Spain
[3] Water Research Institute, University of Barcelona, 08007 Barcelona, Spain
[4] Laboratoire d'Aérologie Université Paul Sabatier, 31400 Toulouse, France
[5] CNRM, University of Toulouse, METEO-FRANCE, CNRS, 38400 Toulouse, France
* Correspondence: joan.bech@ub.edu

Abstract: A methodology to process radar wind profiler Doppler spectra is presented and implemented for an UHF Degreane PCL1300 system. First, double peak signal detection is conducted at each height level and, then, vertical continuity checks for each radar beam ensure physically consistent measurements. Second, horizontal and vertical wind, kinetic energy flux components, Doppler moments, and different precipitation-related variables are computed. The latter include a new precipitation type estimate, which considers rain, snow, and mixed types, and, finally, specific variables for liquid precipitation, including drop size distribution parameters, liquid water content and rainfall rate. The methodology is illustrated with a 48 h precipitation event, recorded during the Cerdanya-2017 field campaign, carried out in the Eastern Pyrenees. Verification is performed with a previously existing process for wind profiler data regarding wind components, plus precipitation estimates derived from Micro Rain Radar and disdrometer observations. The results indicated that the new methodology produced comparable estimates of wind components to the previous methodology (Bias < 0.1 m/s, RMSE ≈ 1.1 m/s), and was skilled in determining precipitation type when comparing the lowest estimate of disdrometer data for snow and rain, but did not correctly identify mixed precipitation cases. The proposed methodology, called UBWPP, is available at the GitHub repository.

Keywords: hydrometeor type estimation; Doppler; wind profiler; pulsed radar

Citation: Garcia-Benadi, A.; Bech, J.; Udina, M.; Campistron, B.; Paci, A. Multiple Characteristics of Precipitation Inferred from Wind Profiler Radar Doppler Spectra. *Remote Sens.* **2022**, *14*, 5023. https://doi.org/10.3390/rs14195023

Academic Editors: Yingzhao Ma, V. Chandrasekar, Robert Cifelli and Seppo Pulkkinen

Received: 11 August 2022
Accepted: 2 October 2022
Published: 9 October 2022

1. Introduction

Radar wind profilers (hereafter RWPs) are designed to retrieve the vertical profile of the wind, through processing Doppler spectra, typically using wavelengths between 20 cm to 6 m, where attenuation by rain can be considered negligible. Bragg and Rayleigh backscattering at these wavelengths, respectively, allows detection of atmospheric echoes caused by both clear air and hydrometeor particles, respectively [1,2]. Depending on the operating frequency, RWPs are often classified as Very High Frequency (VHF band, from 30 MHz to 300 MHz) and Ultra-high frequency (UHF band, from 300 MHz to 3 GHz). In recent decades, RWP networks have been deployed, and routinely operated, in different countries and regions, such as the USA (NOAA Profiler Network, [3]), Europe (COST-76 Action Program) [4], Japan (WINDAS) [5], Korea (KMA) [6] and China (CMA) [7].

The use of RWP includes a wide range of applications, such as evaluation of boundary layer conditions [8,9] diagnostic studies of convective clouds [10,11], windshear and turbulence in complex terrain [12,13] or, in recent years, assimilation into NWP models [14–17]. One key aspect of RWP data processing is the effect of precipitation particles in the sampled volume [18–20], which needs to be taken into account; particularly, to obtain the vertical component of the wind. In fact, previous studies, based on vertical wind components observed by RWP, estimated height of snow or precipitation rate [21,22], but, to our best

knowledge, very limited attention has been devoted so far to the use of RWP observations in retrieval of explicit precipitation types. To fill this gap, the objective of this paper is to describe a new processing methodology for RWP data, addressing, specifically, the detection of precipitation particles and their classification into a simplified precipitation type classification, including rain, snow, and mixed classes. While other instruments, such as conventional polarimetric weather radars, may provide a more complete description of hydrometeor types [23–25], we illustrate the benefits of a simplified classification with RWP data with data sets recorded during the Cerdanya-2017 field campaign in the Eastern Pyrenees mountains.

The verification of results is performed in two stages. First, results of the new method (vertical and horizontal wind) are compared with an already existing processing for RWP. Then, we use Micro Rain Radar (providing profiles of estimated precipitation type) and disdrometer observations (with ground level automatic observations of precipitation type) to produce verification statistics of rain, snow, and mixed precipitation estimates.

The structure of the rest of the paper is as follows. Section 2 describes briefly the Cerdanya-2017 field campaign instruments used in this study. Then, the new processing of RWP data is described in Section 3 and results are compared with other instruments in Section 4. A discussion is provided in Section 5 and conclusions and final remarks are presented in Section 6.

2. Field Campaign and Instrumentation

This section provides, first, a brief overview of the field campaign, region and period of study, and, then, a description of the instruments used in the study.

2.1. Cerdanya-2017 Field Campaign

The datasets used in this study were recorded during the Cerdanya-2017 field campaign, carried out during the 2016–2017 winter season in the Eastern Pyrenees, close to the Spanish, French and Andorra borders (Figure 1). The purpose of the campaign was to study different cold season meteorological phenomena influenced by complex terrain, including cold-pools, mountain waves, and orographic precipitation [13,26]. Instruments used were an UHF RWP, a Micro Rain Radar (MRR2), a disdrometer, and two automatic weather stations (AWSs). The MRR2, disdrometer, and AWS SO were installed in the Das aerodrome (see Table 1), or in the vicinity of about 2.6 km from the MRR2 (Wind Profiler and AWS S8). The instruments were around 1100 m above sea level, surrounded by mountains, with some peaks slightly exceeding 2900 m. One key difference between the RWP and the MRR is the sensitivity, which is much higher for the RWP. Sensitivities were calculated following the method described by [27], as shown in Table 2, along other characteristics explained in more detail in the following subsections.

Table 1. Location of instruments used.

Instrument (Institution)	Longitude (°)	Latitude (°)	Height ASL (m)
RWP (Météo-France)	1.83759 E	42.39688 N	1079
MRR2 (University of Barcelona)	1.86650 E	42.38643 N	1099
Disdrometer (University of Barcelona)	1.86655 E	42.38643 N	1101
AWS S0 (Meteorological Service of Catalonia)	1.86640 E	42.38605 N	1097
AWS S8 (Météo-France)	1.82980 E	42.39340 N	1088

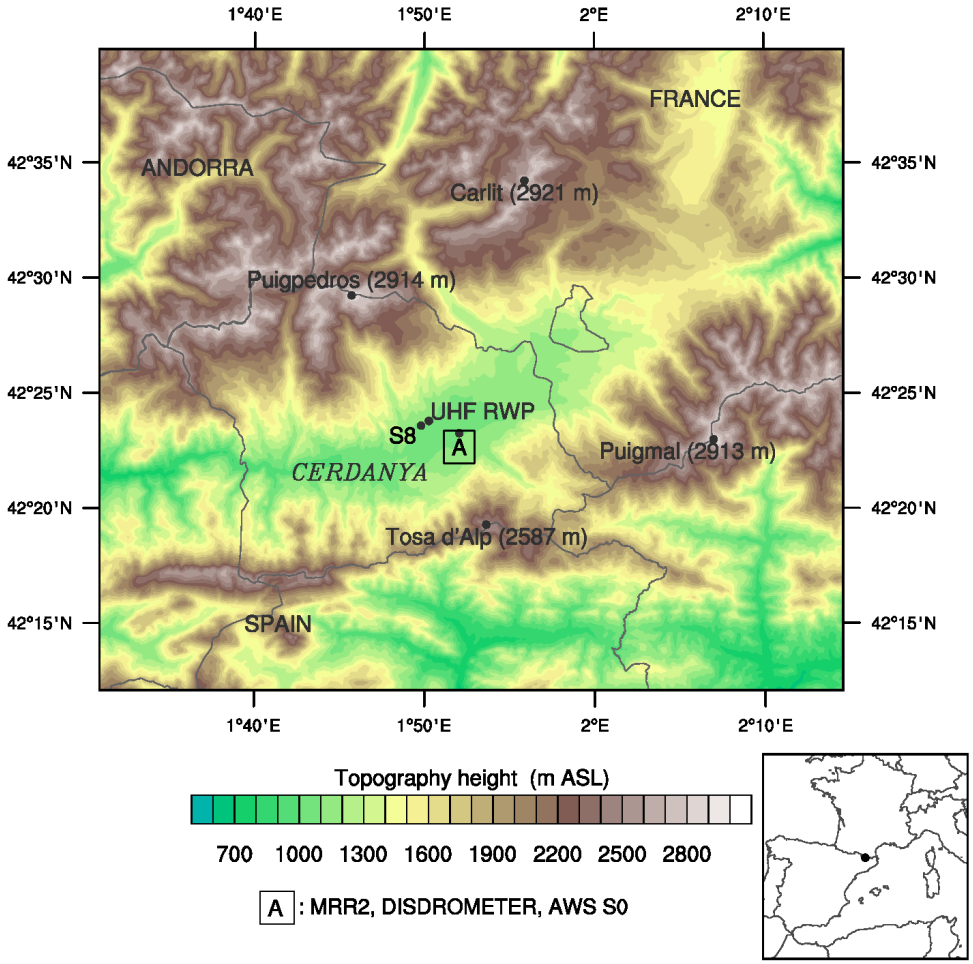

Figure 1. Topography of the Eastern Pyrenees region of study showing the location of the aerodrome (A) with most of the instrumentation: Micro Rain Radar (MRR2), Disdrometer and AWS from the Meteorological Service of Catalonia. Location of an additional Météo-France AWS (number S8) and the Ultra-High Frequency wind profiler (UHF RWP). The main mountain peaks of Carlit (2921 m ASL), Puigpedrós (2914 m ASL) and Puigmal (2913 m ASL) are also labelled, as well as Andorra, France and Spain and their borders.

Table 2. Main features of the RWP and MRR2 used in this study.

Feature	RWP	MRR2
Manufacturer, model	Degreane, PCL1300	Metek, MRR2
Frequency (GHz)	1.247	24.23
Radio band	UHF	K
Number of range gates	45	32
Number of Doppler bins	128	64
Peak power (W)	2500	0.05
Pulse width (μs)	1	—
Maximum height (km)	6.5	3.1
Minimum reflectivity at 1 km (dBZ)	−15.0	−4.7

The data used in this paper were recorded during a 48 h period, from the 24th to 25th of March 2017. This period was selected because it contained different regimes of precipitation (stratiform and convective), alternating also at different ground level hydrometeor types (with snow and rain transitions). Total precipitation recorded at AWS S0 during the event was 30 mm. Complementarily, a second three-day event (3 to 5 February 2017) also

containing different precipitation types at ground level, was examined, and can be found in the Supplementary Materials.

2.2. UHF Wind Profiler

We used a RWP model PCL1300, manufactured by the French company Degreane (see Table 2 for technical details), configured with five fixed antennas and two operating modes, depending on the pulse length used, high and low. In high mode, the range gate length was 187.5 m and the first gate was at 102 m above ground level (AGL), reaching 9102 m AGL. In low mode, the gate length was 150 m and the first gate was at 96 m AGL, reaching 6696 m AGL. In order to have the maximum vertical resolution possible, RWP data used here corresponded only to low mode. The complete update cycle of measurements was about 3 min, but, as mentioned below, the verification of precipitation type was performed averaging measurements into 5-min resolution data.

The five-beam configuration of the unit is illustrated in Figure 2. One beam was oriented vertically, and the other four were tilted towards the cardinal directions, each with the same zenithal angle (17°, i.e., with an elevation angle of 73° over the local horizontal plane). The vertical beam is numbered as beam 1 and the four beams in the cardinal directions (North, South, East and West) are numbered 2, 3, 4 and 5, respectively. Each beam has an angular width of 8.5°.

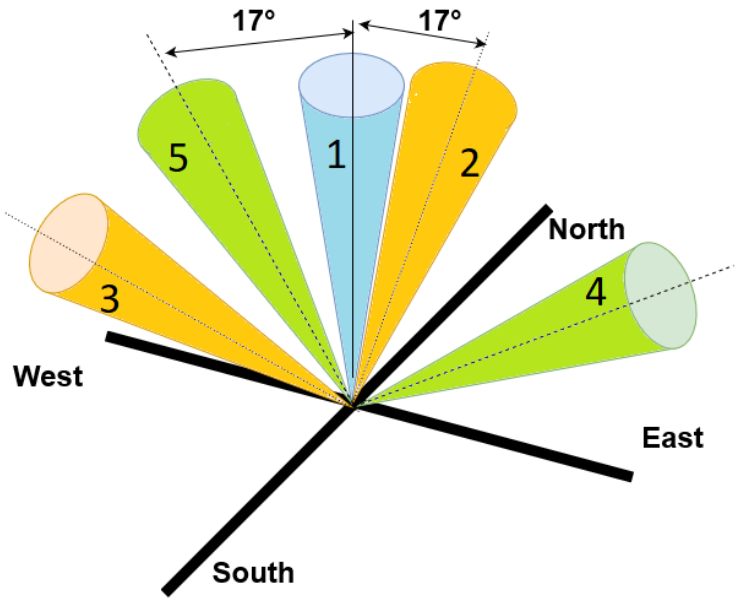

Figure 2. Scheme of wind profiler five-beam configuration with a vertical beam (blue) and four tilted beams oriented towards the four cardinal directions with constant zenithal angle (17°, not to scale). Each beam is numbered according to the labels shown (1, 2, . . .).

The manufacturer data acquisition software applied rain detection on vertical speed and reflectivity criteria to avoid speed aliasing and receiver saturation. In particular, when an abrupt increase in vertical speed was detected, the system increased the Nyquist velocity and changed speed spectra resolution from 0.18 m/s to 0.30 m/s, and the output data included a flag named *Pluie* (rain flag, in this paper).

RWP Doppler spectra of each beam were stored in raw data files (so-called .dat Degreane files). Typically, these files were processed with a methodology developed at the *Laboratoire d'Aérologie* of the *Université Paul Sabatier*, the Aerologie Laboratory Wind Profiler Processing (ALWPP), including signal peak detection and spectrum filtering, as described in [28]. The output files were processed by Météo-France and stored in netcdf files. These data are referred to, hereafter, as Method1, and contain, among other variables, horizontal and vertical wind components.

It should be noted that ALWPP was developed to retrieve wind profiles (horizontal and vertical components) plus additional rainfall variables, such as kinetic energy fluxes used for erosion studies. However, ALWPP does not contain a hydrometeor classification, unlike the proposed UBWPP. For this reason, a comparison between ALWPP and UBWPP was performed covering only wind components, but no other variables were compared with other instruments, as described below.

2.3. Micro Rain Radar

A Micro Rain Radar [29], model MRR2 (hereafter MRR2), manufactured by the German company Metek GmbH, was used. It is a frequency modulated continuous wave, vertically pointing, Doppler radar operating at K band, suitable for precipitation measurements [30]. The unit has 32 range gates and was configured with a range gate vertical resolution of 100 m, starting at 100 m AGL and reaching 3.2 km AGL–see Table 2 for a summary of technical details. Doppler spectra of each range gate were processed with the methodology described in [10], which included the computation of Doppler fall speed, equivalent radar reflectivity, and precipitation type (drizzle, rain, snow, mixed, and hail), among other variables. Vertical MRR2 profiles were available with 1-min resolution.

2.4. Disdrometer

A laser disdrometer. manufactured by the German company OTT GmbH, model Parsivel2 [31], was also used in this study. It provided particle size and fall speed spectra at ground level, and a number of derived variables, which included precipitating hydrometeor type, coded according to the World Meteorological Organization (WMO) Table 4677 specifications (WMO 2018 [32]). Disdrometer hydrometeor types were available with 1-min resolution.

2.5. Automatic Weather Stations

Two automatic weather stations (hereafter AWSs) from Météo-France and the Meteorological Service of Catalonia were also used. They provided, with 1-min temporal resolution, temperature and relative humidity measurements. These two variables were used to compute the probability of snow (assuming precipitation was present), based on the empirical formula proposed by [33], and the thresholds determined by [34,35] to distinguish rain, mixed, and snow cases. The ranges of probabilities were 0.00 to 0.39 (rain), 0.40 to 0.58 (mixed), and 0.59 to 1.00 (snow).

3. Data Processing

This section describes the new processing methodology, the University of Barcelona Wind Profiler Processing (UBWPP). Input data are the raw Doppler spectra power encoded in the so-called RWP .dat Degreane files. Further technical details about the file format are available in the Supplementary Materials, such as the RWP parameters, the automatic configuration of the RWP and signal decoding.

The main processing steps of UBWPP are detailed in Figure 3, including Signal Peak Detection, Vertical Continuity Check and Parameter Calculation. Note that the first two steps were applied to all five RWP beams, as previous methods used in radar wind profiler processing, have done [36,37].

3.1. Signal Peak Detection

The detection of signal peaks was performed for each range of height beam at a given time instant, where the signal was examined as a function of the Doppler spectrum. With the method used, at most, two maximum values were detected. A maximum value followed the definition of the signal adjusted with the convolution method [38] with smoothing filter, where the signal was adjusted to a smoother signal, but with well-defined maxima. It is important to note that at this point the rate of fall and its moments were calculated, so the value of the signal was not relevant (see Supplementary Materials). As illustrated

in Figure 4, starting from the original signal (Figure 4a) a convolution was performed (marked in red in Figure 4b), and, based on this, two modes at most were identified. The inflection points of these modes were used to identify the velocity interval of the signal identified. The resulting signal identified is shown in red in Figure 4c (the blue part of the signal was rejected). Note that the area below the identified signal was used to compute the equivalent reflectivity.

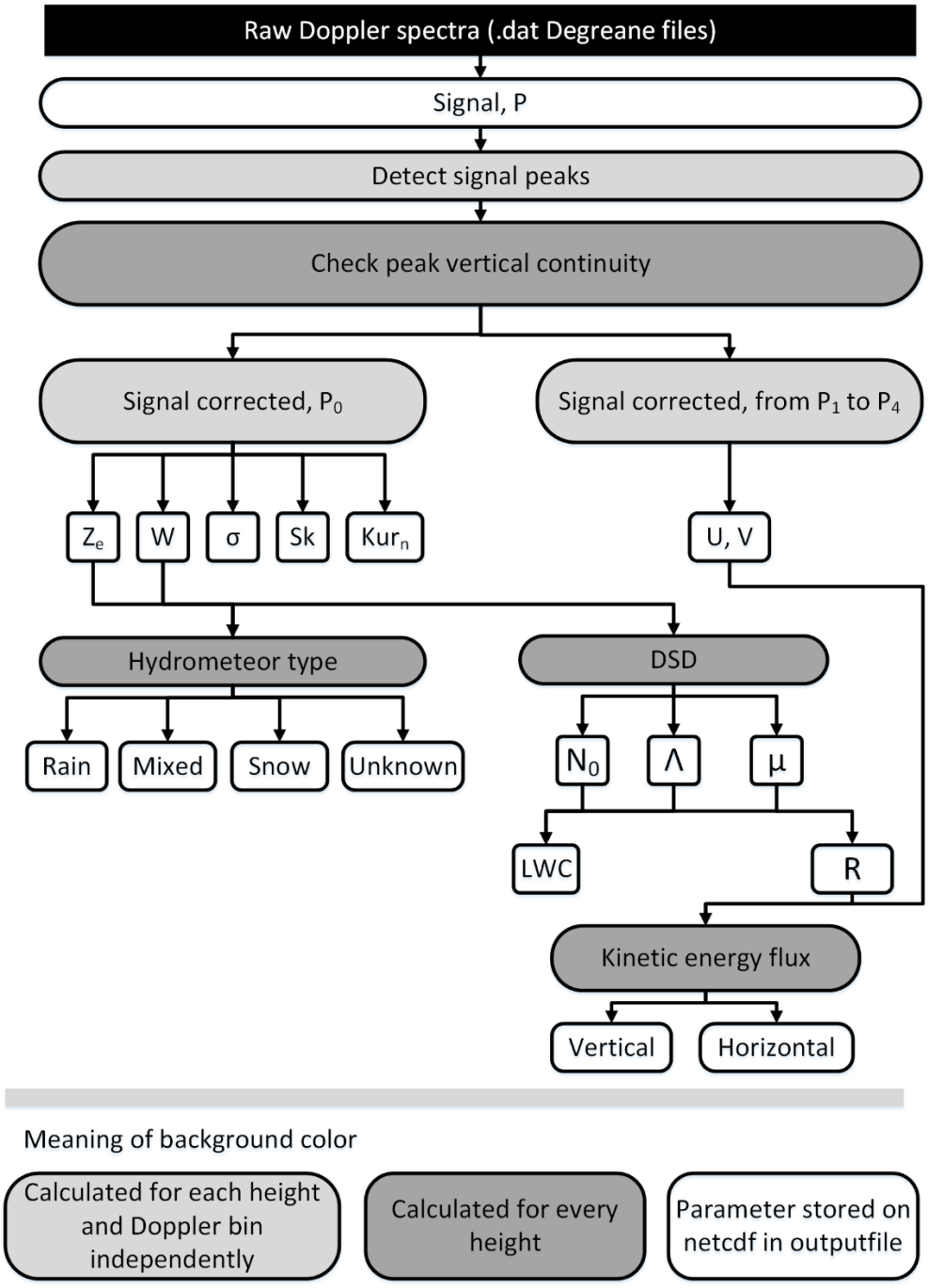

Figure 3. Flow diagram of the UBWPP Wind Profiler processing of raw Doppler spectra and output variables, see in the text for the explanation of the parameters appearing in the diagram.

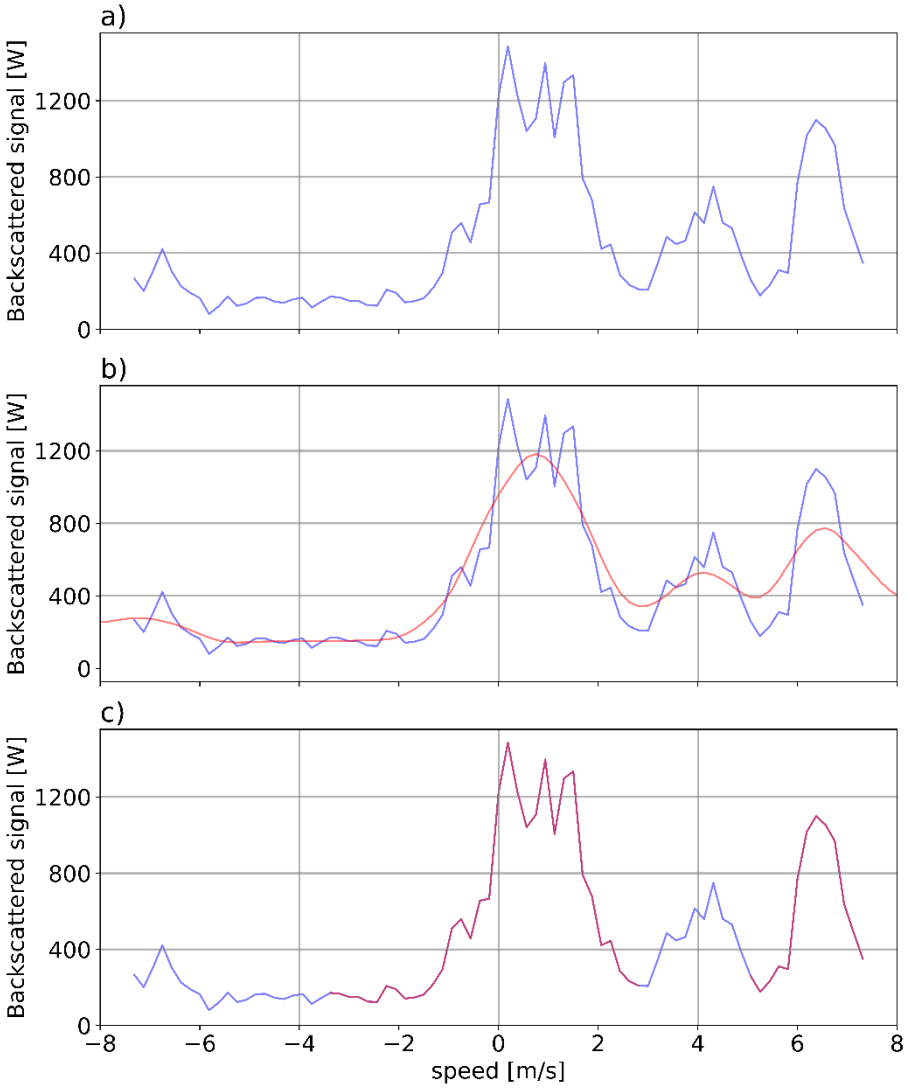

Figure 4. Signal peak detection on a vertical beam: (**a**) original signal, (**b**) convolution (in red) and original signal (in blue) (**c**) result, where part of the original signal was refused (in blue) and the rest (in red) was the corrected signal. At most two peaks were kept from the original signal. Data corresponds to Beam number 1 (vertical incidence, positive values corresponding to downward movement).

Despite this scheme considering a maximum of two peaks, which, in principle, could allow finding the true terminal velocity of hydrometeor particles in convective updrafts by simple subtraction, this was finally not implemented. The reason was that a wide variety of situations were found for both precipitation and non-precipitation Doppler spectra, for example, rain with one peak or clear-air with two peaks. Therefore, the peak spectra allowed more precise calculations (for example, of Doppler moments) but they were not used to attempt to compute true terminal speeds of hydrometeors. The process of signal peak detection illustrated in Figure 4 was not only applied to Beam 1 (vertical velocities) but to all other beams (Beams 2, 3, 4, and 5).

Considering the noise level as the minimum value from the backscattered signal, and the signal-to-noise ratio (SNR) as the ratio between the maximum signal detected by the noise detected, then:

$$SNR = 10 \cdot \log_{10} \frac{Signal_{max}}{Noise}, \quad (1)$$

3.2. Vertical Continuity Check

A check on the vertical continuity of the peak found on the previous step was performed to avoid jumps in the vertical velocity profile. These variations might be due to a malfunction, or the detection of non-meteorological targets (birds or insects). A threshold value was detailed to give physical meaning to the profile, where the speed found at one height could not exceed the limit of 5 m/s at the adjacent height. The height range in high mode was 187 m and in low mode 150 m, so, assuming this limit was deemed reasonable. An example of this process is illustrated in Figure 5, showing first the original signal (with amplitude normalized) at each height, then the peak detection, and, finally, the vertical continuity test applying the threshold mentioned above. Despite the vertical continuity test having been described explicitly for Beam 1, it was also applied to all other beams.

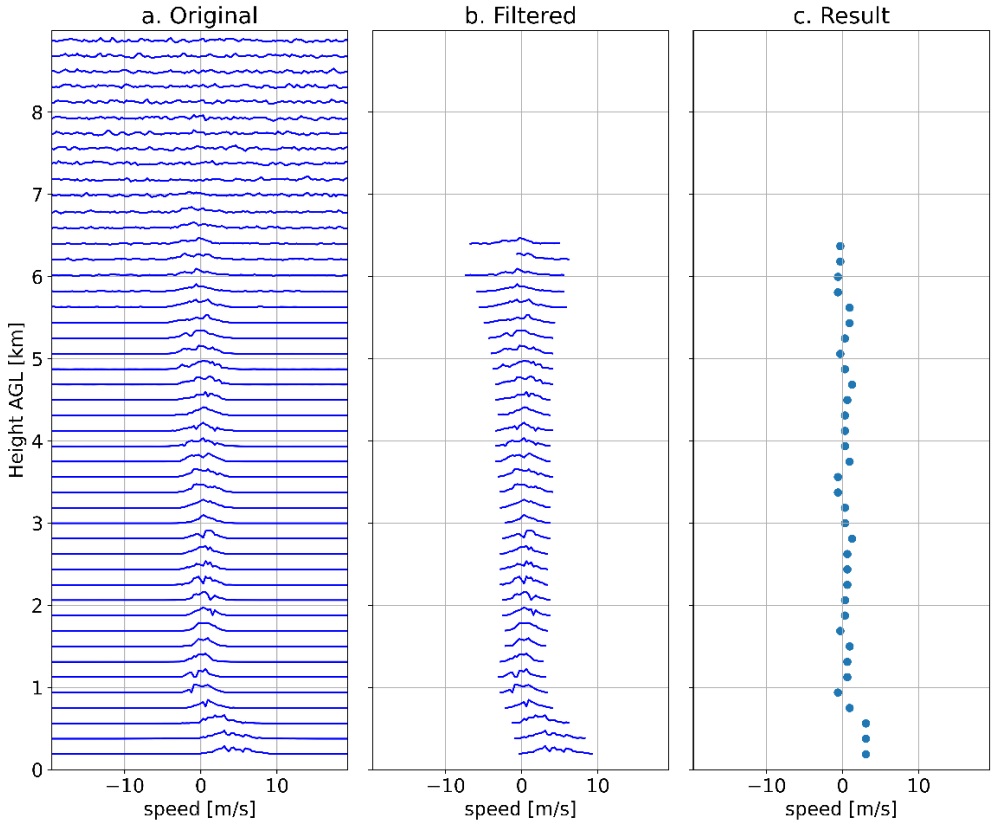

Figure 5. Example of Doppler speed profile corrected with the RWP vertical continuity test: (**a**) original signal, normalized, at each height; (**b**) signal after the peak detection was performed; (**c**) mean vertical speed for each height after applying the vertical continuity test. Data corresponds to Beam number 1 (vertical incidence, positive values corresponding to downward movement) recorded on the 25th of March 2017 3:01:44 UTC.

3.3. Parameters Calculation

Several derived parameters, including three-dimensional Wind Components, Radar Reflectivity, Drop Size Distribution, Liquid Water Content, Kinetic Energy flux, and Hydrometeor Type were calculated. Additional information about the formulae used for Doppler moments are provided in the Supplementary Materials.

3.3.1. Wind Components

In this process the radial speed was calculated for each beam, assuming the wind was constant at a given altitude during the measurement period. The relation between zonal (u), meridional (v), and vertical (w) velocity components are given by:

$$v_{r,1} = w, \tag{2}$$

$$v_{r,2} = -\cos\alpha_2 \cdot v + \sin\alpha_2 w \tag{3}$$

$$v_{r,3} = \cos\alpha_3 \cdot v + \sin\alpha_3 w \tag{4}$$

$$v_{r,4} = -\cos\alpha_4 \cdot u + \sin\alpha_4 w \tag{5}$$

$$v_{r,5} = \cos\alpha_5 \cdot u + \sin\alpha_5 w \tag{6}$$

where α_i is the angle between the vertical and the beam i, with $i = 1, \ldots 5$ according to the beam numbering described in Section 2.2., and downward vertical velocity was defined as positive.

Note that if the angle for all beams was the same, then:

$$v = \frac{v_3 - v_2}{2 \cdot \cos\alpha} \tag{7}$$

$$u = \frac{v_5 - v_4}{2 \cdot \cos\alpha} \tag{8}$$

$$w = v_1 = \frac{v_2 + v_3}{2 \cdot \sin\alpha} = \frac{v_4 + v_5}{2 \cdot \sin\alpha} \tag{9}$$

According to the last equations, the vertical speed w could be obtained 3 different ways; although UBWPP only used the direct measurement from Beam 1.

3.3.2. Radar Reflectivity

The frequency of the WPR was 1274 MHz so the wavelength was around 0.23 m and the Rayleigh scattering regime was valid for cloud droplets and raindrops. The radar reflectivity was calculated from the power received, once filtered. Equation (10) shows the radar reflectivity Z from Beam 1 (vertically pointing):

$$Z(dBZ) = 10 \cdot \log_{10} P_r - Ct + 20 \cdot \log_{10} h, \tag{10}$$

where P_r is the received power, Ct is related to the radar constant RC ($Ct = 10\log_{10}(RC)$) previously known, and h is the height above ground level, assuming the antenna height is negligible.

3.3.3. Precipitation Type

Prior to estimating the precipitation type it was necessary to distinguish clear air echoes from precipitation echoes. Therefore, a precipitation detection procedure was applied, consisting of the verification of at least one of the two following conditions: (i) the rain flag; (ii) the signal to noise ratio of the peak detected (see Section 3.1) exceeding 10 dB.

Once a precipitation echo was detected we proposed two approaches for the evaluation of the precipitation type, considering in both the following simplified classes, based o thermodynamic phase: rain (including liquid precipitation), snow (including solid precipitation) and mixed (including both solid and liquid precipitation), and unknown (when none of the former classes was detected).

The first approach was based on Atlas et al. (1973) [39] (hereafter A73) and it classifies precipitation considering the observed vertical velocity w and spectral width σ given for each hydrometeor type, according to the expected terminal velocity values for rain

v_{rain} and snow v_{snow} particles obtained from the reflectivity, as described in [39]. The equations are:

$$v_{rain} = 2.65 \cdot Z^{0.114} \quad (11)$$

$$v_{snow} = 0.817 \cdot Z^{0.063} \quad (12)$$

where velocities are expressed in m s^{-1} and Z in mm^6 m^{-3}. The method is modified to include the mixed case, containing both solid and liquid precipitation.

The second approach was based on the threshold values for different hydrometeors reported in Ralph et al. 1995 [40] (hereafter R95) where the values were modified to include the mixed case. The thresholds are detailed in Table 3.

Table 3. Precipitation type adapted from A73 and R95.

Approach	Type	Condition
A73	Rain	$\lvert v_{rain} - w \rvert < 2 \cdot \sigma$ *and* $\lvert v_{snow} - w \rvert > 2 \cdot \sigma$
	Mixed	$\lvert v_{rain} - w \rvert < 2 \cdot \sigma$ *and* $\lvert v_{snow} - w \rvert < 2 \cdot \sigma$ *and* $v_{rain} \geq w \geq v_{snow}$
	Snow	$\lvert v_{rain} - w \rvert > 2 \cdot \sigma$ *and* $\lvert v_{snow} - w \rvert < 2 \cdot \sigma$
	Unknown	*None of the above*
R95	Rain	$w \geq 3$ m s^{-1} *and* $\sigma^2 \geq 1$ m^2 s^{-2}
	Mixed	2 m $s^{-1} \leq w \leq 3$ m s^{-1}
	Snow	0.5 m $s^{-1} < w < 2$ m s^{-1} *and* $\sigma^2 < 1$ m^2 s^{-2}
	Unknown	*None of the above*

Despite both A73 and R95 echo precipitation classifications originally using different initial variables and final precipitation classes they both rely on comparing the Doppler velocity spectrum measured at vertical incidence with terminal velocity of precipitation particles. With our proposal we tried to adapt this approach considering also a mixed precipitation class, including solid and liquid precipitation.

3.3.4. Drop Size Distribution

For precipitation echoes classified as rain, the drop size distribution N(D) was computed assuming a gamma distribution [41]:

$$N(D) = N_0 \cdot D^{\mu} \cdot e^{-\Lambda \cdot D} \quad (13)$$

where D is the drop diameter (in m), N_0 is the intercept (in $m^{-(\mu+4)}$) that can be interpreted as the number density per unit drop diameter, Λ is the slope (in m^{-1}) associated with the gradient of the distribution, and μ the shape parameter (dimensionless). This last parameter follows the quadratic expression derived by [42] as explained in [28]:

$$\Lambda = 50.0 \cdot \mu^2 + 1200.0 \cdot \mu + 3390.0 \quad (14)$$

As the shape parameter μ has no analytical equation, it must be solved using the vertical speed, expressed in terms of a_i (from i = 1, 2 and 3) coefficients [43].

$$W(D) = a_1 - a_2 \cdot e^{-a_3 \cdot D} \quad (15)$$

and the mean vertical speed obtained after integration over all diameter from 0 to infinity. In this analysis the vertical air speed is considered negligible.

$$< W > = a_1 - a_2 \cdot \left(1 + \frac{a_3}{\Lambda}\right)^{-(\mu+7)} \quad (16)$$

Thus, the value of μ is calculated using the intersection of two functions (f_1, and f_2), derived from Equation (16). The analytical solution is obtained giving values to μ between -6.9 to 30 with a resolution of 0.01.

$$f_1 = \frac{-1}{\mu + 7} \cdot \ln\left(\frac{a_1 - w}{a_2}\right) \tag{17}$$

$$f_2 = \ln\left(1 + \frac{a_3}{\Lambda}\right) \tag{18}$$

where the units of a_1 and a_2 are m s^{-1}, and for a_3 are m^{-1}. These parameters are function of the density, except a_3:

$$a_1 = 9.65 \cdot \frac{\rho_0}{\rho}^{0.4}, \tag{19}$$

$$\alpha_2 = 10.3 \cdot \frac{\rho_0}{\rho}^{0.4}, \tag{20}$$

$$a_3 = 600, \tag{21}$$

The rain rate R is computed assuming that the mean drop size distribution $N(D)$, follows a gamma function and integrating over all diameters [39]:

$$R = N_0 \cdot \Gamma(\mu + 4) \cdot \frac{\pi}{6} \cdot \left(a_1 \cdot \Lambda^{-(\mu+4)} - a_2 \cdot (\Lambda + a_3)^{-(\mu+4)}\right), \tag{22}$$

3.3.5. Liquid Water Content

The liquid water content (*LWC*) is the liquid water amount contained in a unit volume, which is proportional to the third moment of the DSD. Supposing a spherical shape, the density is ρ_w equal to 10^6 in g m^{-3}, the *LWC* units are g m^{-3}, and is given by:

$$LWC = \rho_w \cdot \frac{\pi}{6} \cdot N_0 \cdot \frac{\Gamma(\mu + 4)}{\Lambda^{\mu+4}} \tag{23}$$

3.3.6. Kinetic Energy Flux

The rain kinetic energy flux crossing a horizontal surface of unit area during a unit of time is decomposed in vertical and horizontal components. The horizontal kinetic energy flux *HKEF* is a function of the horizontal wind speed:

$$HKEF = \rho_w \cdot V^2 \cdot \frac{R}{2} \tag{24}$$

where V is the module of the horizontal wind and R is the rain rate. The unit of *HKEF* is g s^{-3}. The vertical kinetic energy flux VKEF (also in g s^{-3}) is a function of the vertical speed:

$$\begin{aligned} VKEF = \rho_w \cdot N_0 \cdot \Gamma(\mu + 4) \cdot \frac{\pi}{12} \\ \cdot \left[a_1^3 \cdot \Lambda^{-(\mu+4)} - a_2^3 \cdot (\Lambda + 3 \cdot a_3)^{-(\mu+4)} + 3 \cdot a_1 \cdot a_2^2\right. \\ \left. \cdot (\Lambda + 2 \cdot a_3)^{-(\mu+4)} - 3 \cdot a_2 \cdot a_1^2 \cdot (\Lambda + a_3)^{-(\mu+4)}\right] \end{aligned} \tag{25}$$

These equations were derived and used in [28] to estimate rainfall kinetic energy with radar data, complementing previous studies of soil erosion effects of rainfall made with disdrometric measurements [44].

4. Results

The results of the new methodology are illustrated for the Cerdanya-2017 field campaign precipitation case recorded from March 24 to 25th March 2017 [26], where the passage of a warm and a cold front produced several hydrometeor type transitions at ground level alternating with stratiform and shallow convective precipitation.

The verification is described in two distinct parts: wind components and precipitation type.

Wind components were computed with the Aerologie Laboratory Wind Profiler Processing (ALWPP) [28] (Method1), and compared with the new proposed methodology named University of Barcelona Wind Profiler Processing (UBWPP), hereafter Method2. MRR2 data is also used to compare the vertical wind estimates. The purpose of this comparison is to ensure that Method2 is able to properly compute wind components, using Method1 as a benchmark.

Then a comparison of Hydrometeor type obtained with Method2 is performed with MRR2 (profiles), and disdrometer and AWS data (at ground level).

4.1. Vertical Speed

The vertical speed wind component is an essential variable to perform the estimation of precipitation type; therefore, here we compared the average estimates performed with RWP (Method1 and Method2) and MRR2, processed according to [10] and homogenizing both the temporal and spatial resolution to Method1 (Figure 6). Some differences are expected between RWP and MRR2 estimates, due to the different frequencies of operation (UHF vs. K band) and, to a lesser extent in this case, to the siting of the two instruments, given the mostly stratiform character of the event. MRR2 can only observe precipitation particles while RWP detects both precipitation and clear air wind.

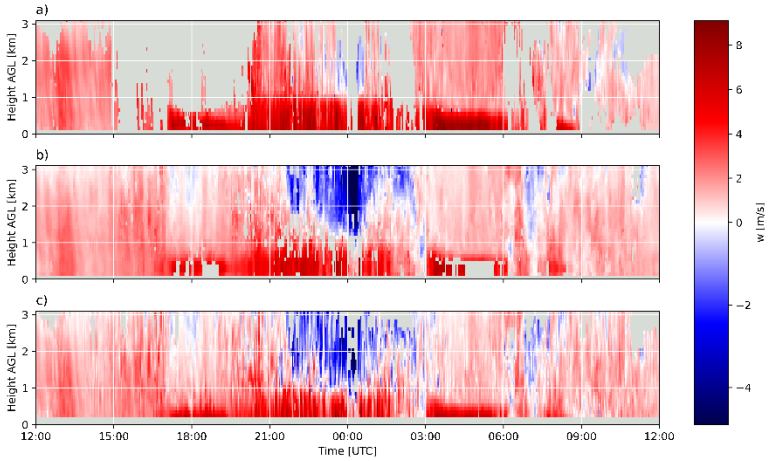

Figure 6. Vertical speed (downward defined positive) estimates for 24th to 25th March 2017. (**a**) MRR2, (**b**) RWP (Method1) and (**c**) RWP (Method2).

Figure 6 shows clear similarities between the estimates of the two instruments and between Method1 and Method2. An overall agreement was found in the pattern distribution, with a clear sharp gradient, indicating a melting layer signature, around 1 km AGL at 00 UTC (more evident for the MRR2, Figure 6a), and also negative speeds (updrafts, in blueish colors) around 00 UTC, much more clearly (in intensity in duration) in both RWP estimates. The better ability of the RWP to observe updrafts was expected for UHF measurements able to measure Bragg backscattering caused by air molecules unlike K band measurements, which only detect updrafts if precipitation particles are present.

A more detailed comparison between Method1 and Method2 is shown in the scatter plot and frequency distributions of Figure 7, distinguishing RWP echoes labelled with the rain flag from the rest. Distribution patterns of rainy and non-rainy conditions for Method1 and Method2 are very similar, unimodal and wider vs bimodal with the main mode centered at 0 m/s, respectively. The global analysis of 29820 points indicated a Mean Error (ME) (Method2–Method1) of −0.04 m/s, a Root Mean Square Error (RMSE) of 0.39 m/s, and a correlation coefficient of 0.86.

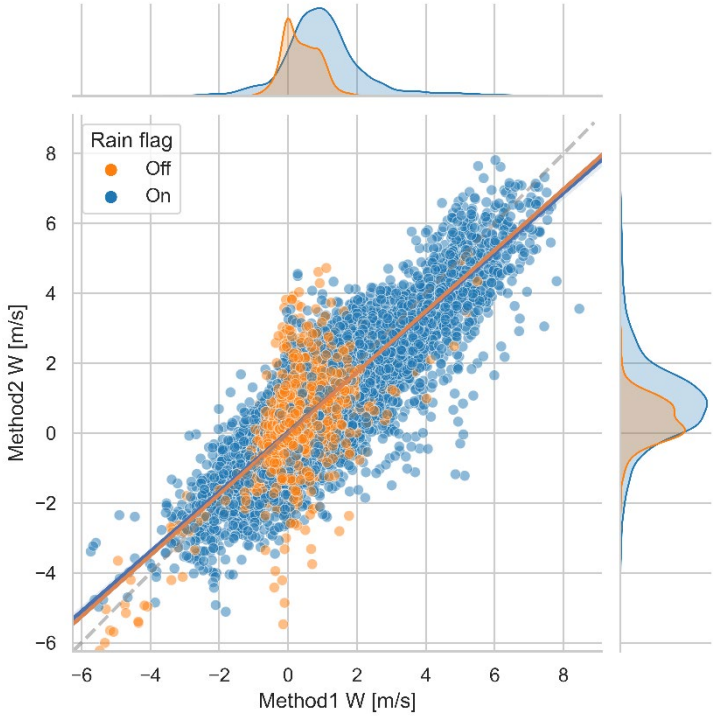

Figure 7. Vertical speed from ALWPP (Method1) vs UBWPP (Method2) showing wind profiler echoes in rainy (20127 samples, in blue) and non-rainy (9693 samples, in orange) conditions, the corresponding linear regression (also in blue and orange) and the diagonal (dashed) line. The top and right panels show the normalized distributions of rainy and non-rainy conditions for Method1 and Method2, respectively.

4.2. Horizontal Wind

Figure 8 shows scatter plots of Method1 vs Method2 for both zonal (U) and meridional (V) wind components (left column) plus histograms of differences between the two methods (right column). Note the similar patterns found in the zonal and meridional distributions and the symmetrical and unbiased (<0.1 m/s) shape of the distributions of differences. Statistical analysis of 24201 samples indicated ME, RMSE and correlation coefficients for zonal (meridional) components of −0.034 m/s, 1.089 m/s and 0.99 (0.088 m/s, 1.154 m/s and 0.96), respectively.

4.3. Precipitation Type

The precipitation type estimation produced with Method2 was evaluated by comparing profiles of equivalent height obtained from MRR2 [10], and ground level disdrometer and AWS data.

Figure 9 provides an overview of precipitation type estimated by the MRR2 (upper panel) and Method2 (lower panel), in this case based on the A73 approach - note that the number of classes was different for each method. The overall pattern was similar, starting with snow (first as virga, reaching the ground around 12 UTC), later with a brief rain shaft and more snow, then (beginning sometime between 16 and 17 UTC) with rain below the melting level and snow above, and finally snow (about 8 UTC). Moreover, a radio-sounding, launched at the Das aerodrome on the 24th of March at 22.34 UTC (see Supplementary Material) indicated that the freezing level was about 0.8 km AGL, consistent with results displayed in Figure 9. The different bin vertical resolution of the two instruments and the distance between them might partly explain the differences in freezing levels. Moreover, despite the general pattern of precipitation types estimated from both instruments being similar, the higher sensitivity of the RWP revealed more precipitation areas, such as those above 0.5 km AGL, from 16 to 20 UTC 24 March 2017.

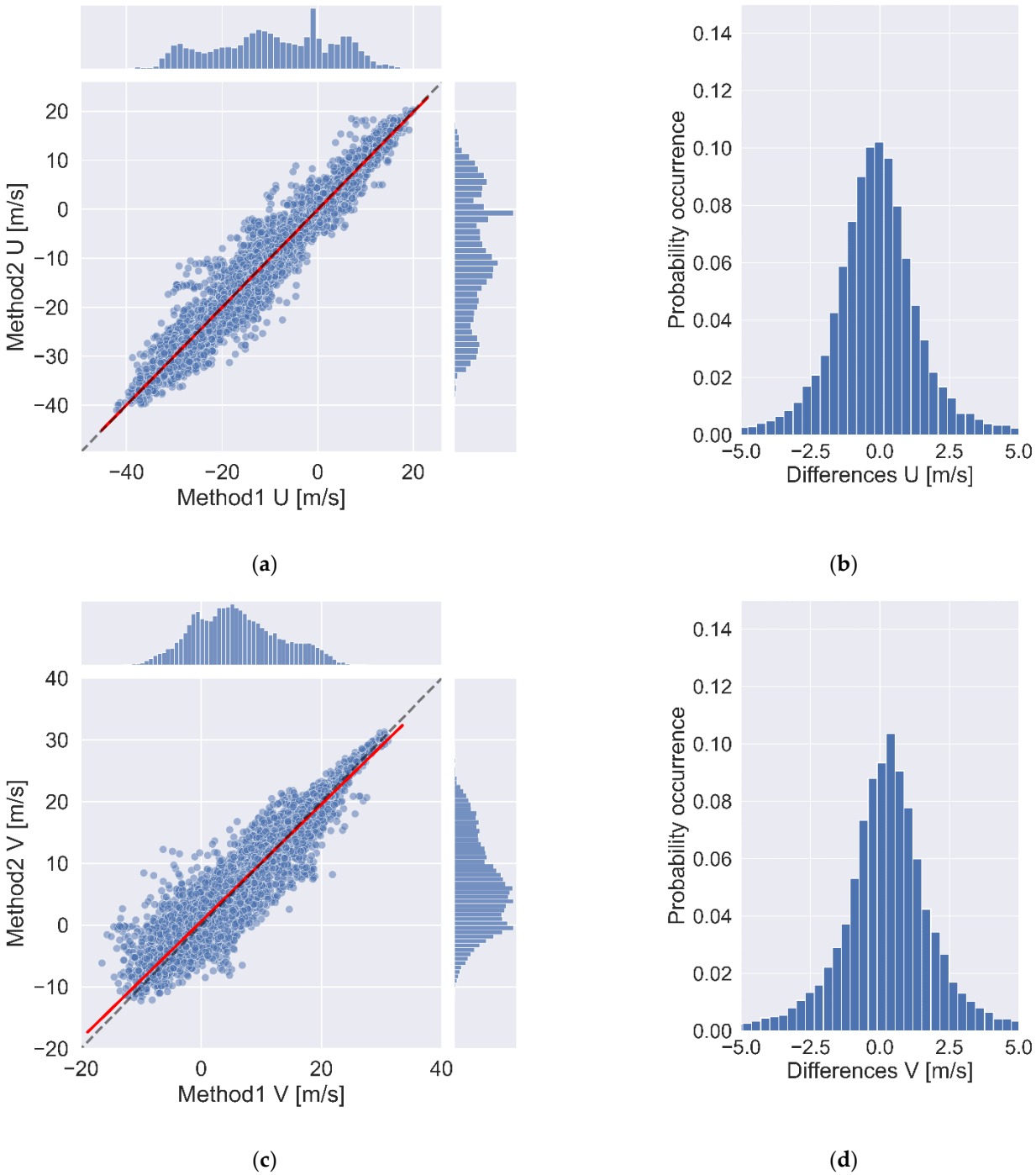

Figure 8. Scatterplots and distributions of differences between ALWPP (Method1) and UBWPP (Method2) for zonal component U, panels (**a**,**b**), and meridional component V, panels (**c**,**d**). Scatter plots show correlation (red) and perfect correlation in diagonal (dashed) lines.

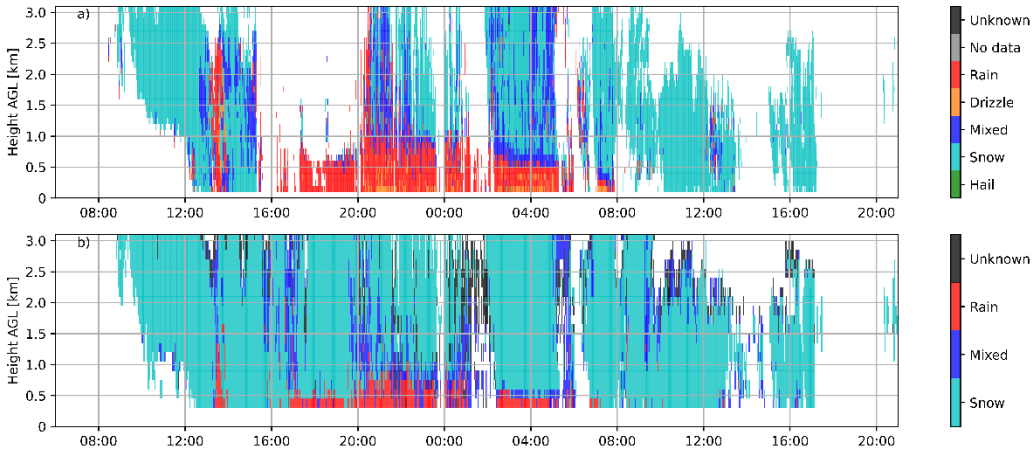

Figure 9. Precipitation type estimation during the 24 and 25 March 2017 event. (**a**) MRR2 observations with 6 classes and (**b**) RWP Method2, using A73, with 5 classes. Note RWP data has been clipped to the MRR2 maximum height. White areas indicate clear air echoes.

A quantitative comparison was performed with disdrometer data and AWS estimates. As Method2 detected five types of precipitation (rain, mixed, snow, no data and unknown) and the disdrometer provided a more complete list of hydrometeor types (WMO Table 4677), the latter had to be properly grouped to perform the comparison. Table 4 lists the WMO codes selected to match the Method2 precipitation types. Note that the Unknown class was assigned to hail, despite this hydrometeor mpt being observed in the datasets examined, so this class should be further verified.

Table 4. Correspondence between precipitation types observed by the disdrometer (WMO Table 4677) and precipitation types estimated with Method2.

Disdrometer Precipitation Type	WMO Table 4677 Values	Method2 Precipitation Type
Drizzle	From 51 to 53	Rain
Drizzle with rain	From 58 to 59	
Rain	From 61 to 65	
Rain, drizzle with snow	From 68 to 69	Mixed
Snow	From 71 to 75	Snow
Snow grains	77	
Soft hail	From 87 to 88	
Hail	From 89 to 90	Unknown

The comparison between Method2 and disdrometer and AWS station data also had to deal with their different temporal resolutions. For practical reasons, Method2 precipitation type, originally with 3.5-min temporal resolution were transformed into 5-min resolution data. Then, AWS and disdrometer data, originally with 1-min resolution, were converted to 5-min resolution with an ad-hoc procedure, described in Appendix A. The number of resulting cases is listed in Table 5.

Table 5. Number of each precipitation type cases for Method2 (A73 and R95) and disdrometer observations after the 5-min time resolution re-binning.

Precipitation Type	Method2 with A73	Method2 with R95	Disdrometer
Rain	113	124	158
Mixed	46	60	37
Snow	118	109	85
Unknown	5	2	-
Total	282	295	280

Finally, to interpret the comparison between the different datasets it must be taken into account that the Das aerodrome (where the MRR2, disdrometer and AWS S0 were) was about 3 km from the RWP site (see Figure 1). Moreover, the lowest RWP precipitation type computed with Method2 was about 300 m above ground level (AGL) and the measures from AWS and disdrometer were about 1.5 m above ground level.

Figure 10 displays the Method2 precipitation type estimated at the lowest range gate (background colors), disdrometer observations, and AWS derived estimates at S0. It was apparent that the overall match was reasonably good, capturing the global initial snow, rain, and final snow periods. AWS S8 provided very similar results (not shown).

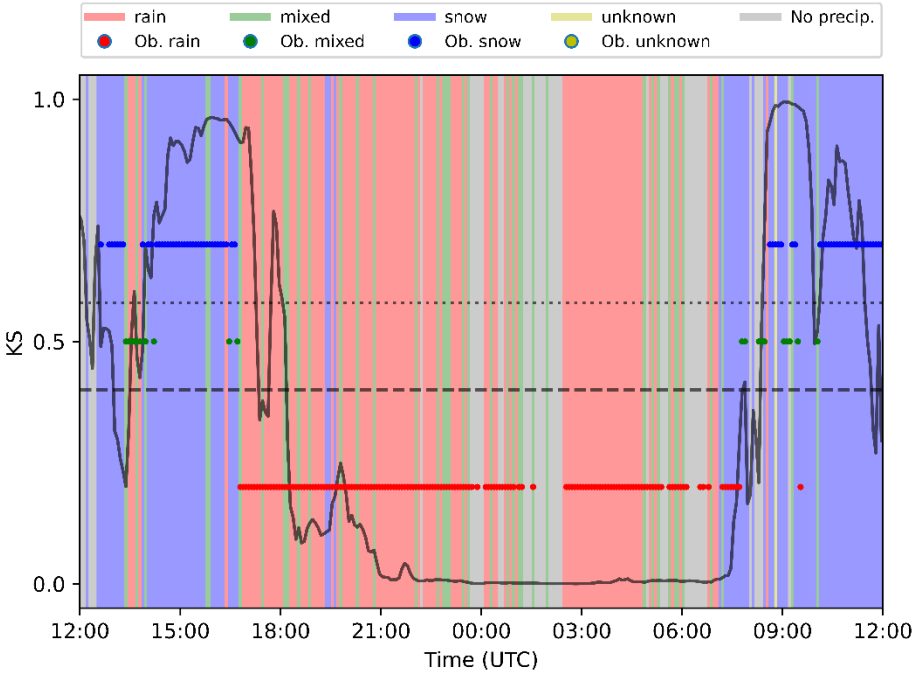

Figure 10. Precipitation type estimated from different sources for the 24 to 25 March 2017 event showing precipitation type estimates from Method2 (vertical, colored stripes), disdrometer observations (small colored circles), and AWS derived Koistinen-Saltikoff (KS) probability of snow (thick black line) at AWS S0 with reference lines for values separating the rain and mixed classes (dashed black line) and the mixed and snow classes (black dotted line). For the sake of simplicity disdrometer colored circles are shown at fixed KS probabilities within the corresponding class.

A quantitative comparison between precipitation type derived from Method2 and disdrometer data was performed with verification scores considering categorical events for the occurrence of the different classes. Scores computed were Probability of Detection (POD), False Alarm Ratio (FAR), Odds ratio skill score (ORSS) and the True Skill Statistic (TSS). A complete description of these scores is given by [45] and formulae used here are detailed in Appendix B.

The quantitative analysis of Method2 precipitation type was performed for both the so-called Atlas and Ralph approaches described in Section 3. For both approaches a range of time windows (additional time before and after the nominal time) were considered in the evaluation, to handle the effect of possible temporal mismatches accounting for the time necessary for the precipitation particle to reach the ground, which could be exacerbated by the presence of strong horizontal wind. Verification scores, considering time windows with intervals of 0, 5, and 10 min, are shown in Table 6 for Rain, Mixed, Snow, and No Precipitation cases.

Table 6. Verification scores of Method2 precipitation type at the lowest height bin compared with disdrometer observations. Time interval windows of 0, 5 and 10 min were considered for both A73 and R95 precipitation type approaches. Perfect values for each verification score are given in parentheses.

Approach	Parameter	Time Interval (min)	POD (1)	FAR (0)	ORSS (1)	TSS (1)
A73	Rain	0	0.78	0.10	0.94	0.68
	Mixed		0.19	0.81	0.41	0.10
	Snow		0.90	0.40	0.93	0.66
	No Precipitation		0.91	0.08	0.98	0.83
	Rain	5	0.79	0.10	0.95	0.70
	Mixed		0.24	0.76	0.57	0.16
	Snow		0.92	0.35	0.95	0.68
	No Precipitation		0.92	0.08	0.98	0.84
	Rain	10	0.79	0.10	0.95	0.69
	Mixed		0.31	0.69	0.68	0.23
	Snow		0.93	0.32	0.95	0.97
	No Precipitation		0.92	0.08	0.98	0.84
R95	Rain	0	0.88	0.05	0.99	0.83
	Mixed		0.33	0.78	0.57	0.21
	Snow		0.77	0.44	0.83	0.54
	No Precipitation		0.88	0.07	0.98	0.81
	Rain	5	0.88	0.05	0.99	0.84
	Mixed		0.55	0.52	0.81	0.44
	Snow		0.82	0.37	0.88	0.60
	No Precipitation		0.89	0.07	0.98	0.82
	Rain	10	0.89	0.05	0.99	0.84
	Mixed		0.59	0.55	0.84	0.48
	Snow		0.83	0.34	0.90	0.62
	No Precipitation		0.89	0.07	0.98	0.82

Results for both A73 and R95 showed skilled distinguishing of No Precipitation echoes, and, therefore, Method2 was able to discriminate between Precipitation and No Precipitation echoes, yielding the best scores of all classes (POD $\geq$ 0.88, FAR $\leq$ 0.07, ORSS $\geq$ 0.98, TSS $\geq$ 0.81). Rain and Snow were reasonably well classified, A73 being better with Snow and R95 with Rain. Mixed types were generally not well classified, with PODs systematically lower than FARs and ORSS and TSS well below 1.

5. Discussion

As seen in Section 4.1., the new methodology UBWPP (Method2) provided very similar estimates of vertical wind component w to those obtained by the existing ALWPP methodology (Method1), with a correlation index of 0.86. Small differences were found, mainly due to signal processing treatment (Method2 being occasionally slightly less sensitive than Method1), and also due to the vertical continuity check (allowing Method2 to detect vertical speeds greater than 6 m/s, undetected by Method1). An example of the

latter can be seen around 5 UTC on 25 March (Figure 6). The comparison of horizontal wind components between Method1 and Method2 also provided very similar results, with correlation coefficients equal to, or greater than, 0.96.

Regarding precipitation impact upon vertical wind components, a key question in this study, the comparison between Method1 and Method2, also showed that, in rainy conditions (Figure 7, rain flag on), the w distribution displayed a double peak, with a main peak close to zero and a secondary peak close to 1 m/s. In non-rainy conditions (rain flag off), the two distributions were unimodal with mode close to 1 m/s (Figure 7). This is a well-known pattern in RWP observations in cases of rain, as air and rain particles exhibit two distinct peaks, confirming that Method2 was able to detect them.

An additional comparison of Method1 versus Method2 horizontal and vertical wind components during a three-day period provided similar results to the case examined here (see Supplementary Materials).

Further insight into the effect of rain on vertical wind estimates is provided by Figure 11, which shows a contour frequency altitude diagram for rainy and non-rainy conditions, where frequency is shown in absolute terms (counts) with a common color scale that allows comparison between the two panels. As expected, in rainy conditions (Figure 11a) the distribution was asymmetric and the Doppler spectra widened, particularly at lower levels (<1 km AGL). This was likely due to the presence of raindrops that, as they approach the ground, increase their size, probably due to collision and coalescence processes either with other raindrops or with lower-level cloud droplets, reaching higher speeds (>5 m/s) and tilting the distribution to positive speeds, with the mode of the distribution (reddish colors) clearly tilted at lower levels (<3 km AGL). On the contrary, non-rainy conditions (Figure 11b) showed a more symmetrical distribution, in this case with slightly longer cues to the right at lower levels consistent with shallow convection, and the distribution mode close to 0 m/s.

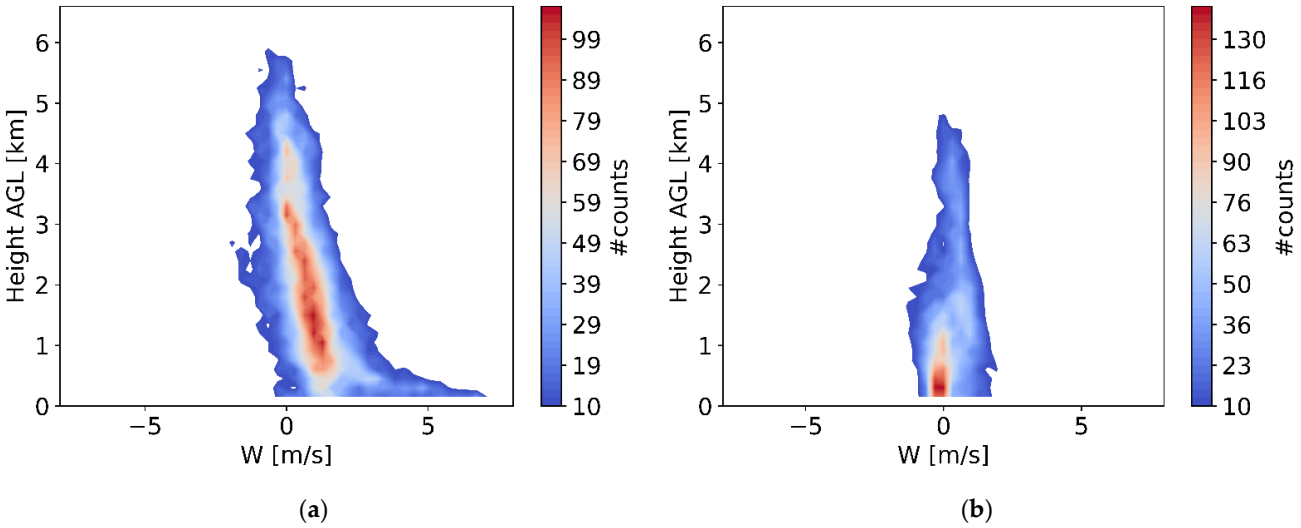

Figure 11. Contour frequency altitude diagram of vertical speed computed with RWP Method2 for 24 to 25 March 2017 considering: (**a**) rainy conditions (rain flag on), (**b**). non-rainy conditions (rain flag off). Frequencies of counts are shown in absolute terms.

The quantitative analysis of Method2 precipitation classification described in Section 4.3. considering two approaches (A73 and R95), provided mostly satisfactory results in terms of verification scores. No Precipitation and Snow echoes were very well identified by A73, with PODs ranging from 0.91 to 0.92 and 0.90 to 0.93, respectively, while for Rain, PODs were a bit lower, 0.78 to 0.79 from A73, and FARs were generally low, not exceeding 0.40 for snow echoes. Mixed echoes were poorly classified, despite the visual

inspection of Figure 9, displaying them in the transition level between snow and rain, as expected. However, both their POD and FAR were unsatisfactory.

The approach based on R95 also provided good results regarding the identification of Rain, Snow, and No Precipitation echoes, with PODs ranging from 0.77 to 0.89 and FARs not exceeding 0.44 for snow echoes. Mixed echoes were better classified than using A73, with PODs ranging from 0.33 to 0.59 and FARs 0.55 to 0.78.

Based on Table 6 (ORSS and TSS scores), A73 performed best at detecting Snow and No Precipitation echoes and R95 provided the best results for rain echoes and Mixed cases, despite the latter still having important deficiencies. Therefore, depending on the application required, one or the other approach might be more advantageous.

The fact that the mixed class at ground level was mostly associated with snow to rain and rain to snow transitions, and the disdrometer and the RWP were not collocated, might have influenced this discrepancy. It should be noted that the mixed class definition based on A73 was successfully tested for MRR2 and the disdrometer collocated during the Cerdanya-2017 field campaign [10].

To further illustrate the event examined, from 24 to 25 March 2017, a selection of variables computed with Method2 and the A73 approach are shown in Figure 12 (radar reflectivity, fall velocity, horizontal wind, and precipitation type). The passage of a warm front with an associated vortex circulation on 24 March was well captured by the wind profile (shifting from south to west) and the onset of precipitation, mostly as rain at ground level. A few hours later, at around 3 UTC 25 March, a cold front brought convective developments (a reflectivity tower exceeding 5.5 km AGL) and stronger eastern winds at all levels, shifting later to the south-west, with the arrival of the colder air mass which implied a transition from rain to snow at ground level. More details of this event can be found in [26].

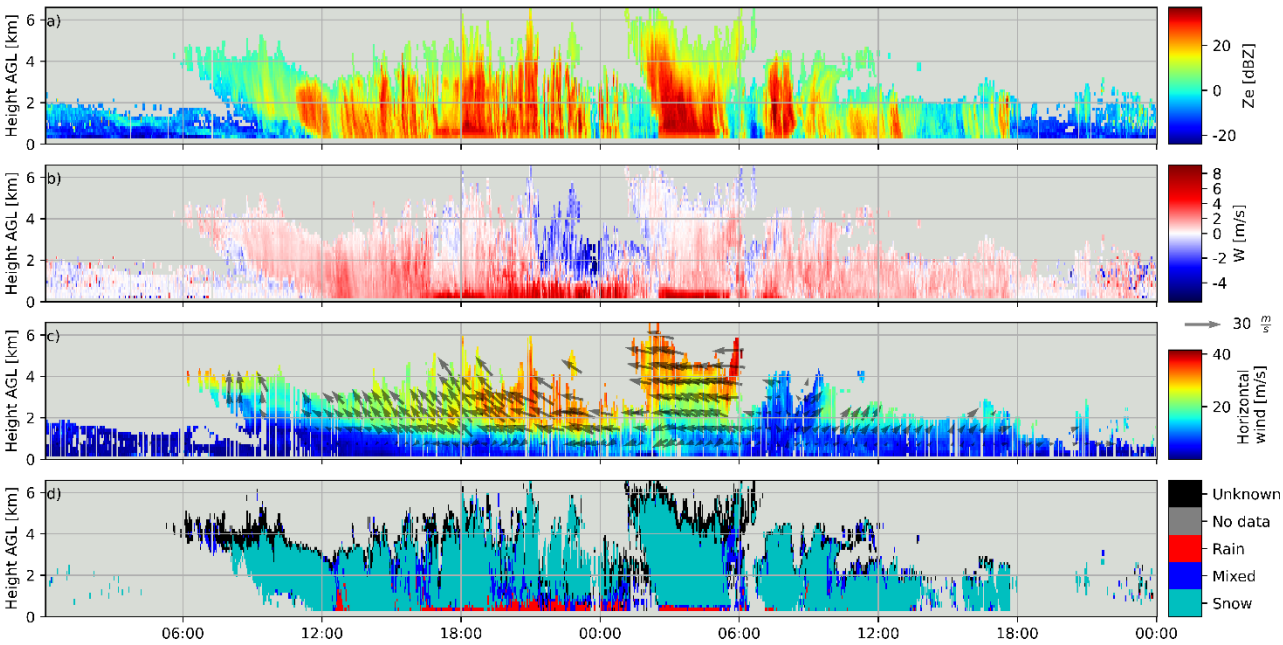

Figure 12. Method2 (A73 approach) processing applied to RWP observations recorded from 24 to 25 March 2017. (**a**) radar reflectivity, (**b**) vertical fall speed, (**c**) horizontal wind, module and direction and (**d**) precipitation type.

6. Conclusions

A new processing methodology of wind profiler Doppler spectra called UBWPP (Method 2) has been described, addressing the computation of horizontal and vertical wind components, and other variables such as radar reflectivity, spectral width, vertical and horizontal kinetic energy, refractive index, liquid water content, drop size distribution

parameters, and a simplified precipitation type classification (including rain, snow, and mixed classes).

The performance of Method2 was assessed using observations of a PCL1300 Degreane UHF wind profiler plus other datasets recorded during the Cerdanya-2017 field campaign. A 48h precipitation event was selected for this purpose as it included different ground-level snow to rain transitions.

Quantitative comparisons with a previously existing methodology to compute horizontal and vertical wind components provided satisfactory results. Nearby disdrometer, automatic weather stations, and Micro Rain Radar observations were used to evaluate the Method2 precipitation type. Despite some limitations in the comparison procedure, qualitative and quantitative results based on contingency table verification scores indicated an overall good performance of the estimated precipitation for snow and rain types showing promise for further application, unlike mixed types, that were not correctly diagnosed.

Future work is planned to review the mixed precipitation class definition and evaluate Method2 with a larger dataset with co-located instruments such as a disdrometer, a Micro Rain Radar, or a polarimetric weather radar. A larger observational data set should be used not only to confirm current results, but also to assess the feasibility of expanding precipitation types; for example, including hail cases.

A version of Method2 written in Python is publicly available at the GitHub repository with the name UBWPP (https://github.com/AlbertGBena/UBWPP (accessed on 30 September 2022)).

Supplementary Materials: The following are available online at https://www.mdpi.com/article/10.3390/rs14195023/s1, Supplementary Material S1: File Header of the Degreane wind profiler PCL1300; Supplementary Material S2: Calculation of selected parameters contained in the Degreane file header; Supplementary Material S3: Decoding of Degreane dat files; Supplementary Material S4: Overview of Radar Wind Profiler Doppler processing; Supplementary Material S5: Moments description; Supplementary Material S6: Evaluation of additional events; Supplementary Material S7: Additional information on 24 March 2017 event.

Author Contributions: Conceptualization, A.G.-B. and J.B.; methodology, A.G.-B. and J.B.; software, A.G.-B., M.U. and B.C.; data curation, A.G.-B.; writing—original draft preparation, A.G.-B. and J.B.; writing—review and editing, A.G.-B., J.B., M.U., B.C. and A.P. All authors have read and agreed to the published version of the manuscript.

Funding: This research was funded by the Spanish Government through projects CGL2015-65627-C3-1-R, CGL2015-65627-C3-2-R (MINECO/FEDER), CGL2016-81828-REDT and RTI2018-098693-B-C32 (AEI/FEDER), and the Water Research Institute (IdRA) of the University of Barcelona.

Data Availability Statement: Data Availability Statement: Data from the Cerdanya-2017 field campaign is publicly available at https://cerdanya.sedoo.fr/catalogue/ (accessed on 8 August 2022).

Acknowledgments: The Cerdanya-2017 field campaign was a research effort organized by the University of the Balearic Islands, the University of Barcelona, METEO-FRANCE and the Meteorological Service of Catalonia (SMC). We thank METEO-FRANCE/CNRM/GMEI/LISA, 4 M and TRAMM teams for the data acquisition during the campaign, especially Jean-Marie Donier from CNRM, and SMC for providing Das automatic weather station data. We also thank deeply the help regarding wind profiler technical processing from Phillip Currier from the company Degreane, manufacturer of the wind profiler used. This research was funded by the Spanish Government through projects CGL 2009-12797-C03-02 and CGL 2009-12797-C03-03 and the Water Research Institute (IdRA) of the University of Barcelona.

Conflicts of Interest: The authors declare no conflict of interest.

Appendix A

This appendix details the method to reclassify the hydrometeor type from disdrometer records, in 1-min resolution, to 5-min resolution, to match the wind-profiler estimates resolution. Figure A1 shows how the five 1-min resolution (m1 to m5) hydrometeor types (Type1 to Type5) are transformed into one of the possible five hydrometeor classes: Rain, Snow, Mixed or No Precipitation. The first possibility considered is that all five 1-min types are the same ("F All Types") which obviously yields the same hydrometeor type. The second one considers the number of rain (R) and snow (S) minutes are the same which produces a Mixed type. The third possibility considers that there are more than three 1-min types equal to no precipitation which produces a No Precipitation type. Then two symmetric groups of conditions are considered in case all 1-min types are not equal to snow or rain, leading to various possibilities. Table A1 lists examples of the hydrometeor reclassification.

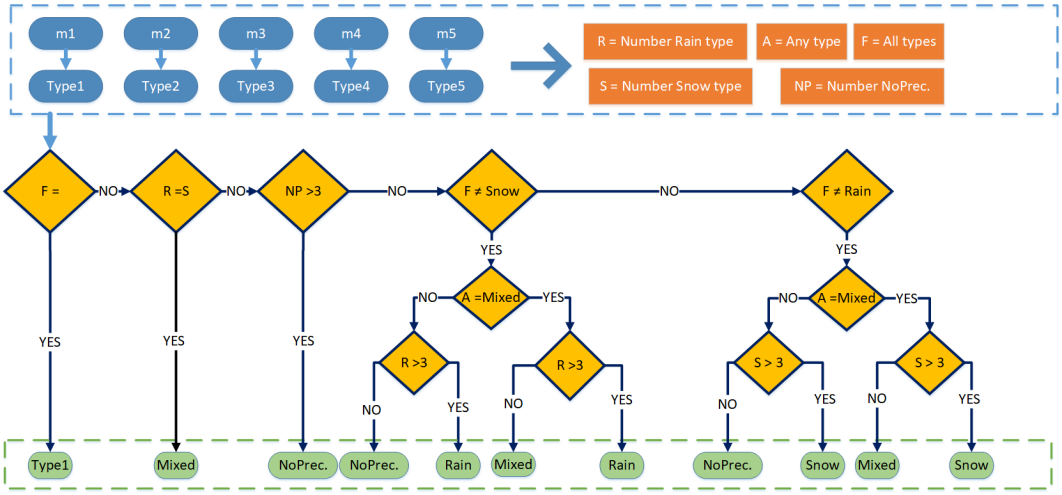

Figure A1. Flow diagram showing the hydrometeor reclassification from 1-min to 5-min periods.

Table A1. Examples of precipitation type reclassification from 1-min to 5-min resolution.

Case	5-min Interval of 1-min Types					Type Chosen
	m1	m2	m3	m4	m5	
1	Rain	Rain	Rain	Rain	Rain	Rain
2	Snow	Snow	Snow	Snow	Snow	Snow
3	Rain	Rain	Rain	Rain	Mixed	Rain
4	Snow	Snow	Snow	Snow	Mixed	Snow
5	Rain	Rain	NoPrec	Snow	Snow	Mixed
6	Rain	Rain	Rain	Snow	Snow	Mixed
7	Snow	Snow	Snow	Rain	Rain	Mixed
8	NoPrec	NoPrec	NoPrec	Rain	Rain	NoPrec
9	Rain	Rain	Rain	Rain	Snow	Mixed
10	Snow	Snow	Snow	Snow	Rain	Mixed
11	Rain	Rain	Rain	Mixed	Mixed	Mixed

Appendix B

The verification scores used are based on a traditional 2 × 2 contingency table where "hits" represent the number of events (precipitation types) correctly forecast, "misses" the number of events not forecast, "false alarms" the number of forecast events that didn't occur and "correct negatives" the correctly forecast events that didn't occur. Scores considered here are Probability of Detection (POD), False Alarm Ratio (FAR), Odds ratio skill score

(ORSS) and the True Skill Statistic, also known as Hanssen and Kuipers discriminant or Peirce's skill score, (TSS), given by the following equations:

$$POD = \frac{hits}{hits + misses} \tag{A1}$$

$$FAR = \frac{false\ alarms}{hits + false\ alarms} \tag{A2}$$

$$ORSS = \frac{hits \cdot Correct\ negatives - misses \cdot false\ alarms}{hits \cdot Correct\ negatives + misses \cdot false\ alarms} \tag{A3}$$

$$TSS = \frac{hits}{hits + misses} - \frac{false\ alarms}{Correct\ negatives + false\ alarms} \tag{A4}$$

References

1. Yamamoto, M. New Observations by Wind Profiling Radars. In *Doppler Radar Observations—Weather Radar, Wind Profiler, Ionospheric Radar, and Other Advanced Applications*; Bech, J., Chau, J., Eds.; InTech: London, UK, 2012; ISBN 978-953-51-0496-4.
2. Lehmann, V.; Brown, W. Radar Wind Profiler. In *Springer Handbook of Atmospheric Measurements*; Foken, T., Ed.; Springer: Cham, Switzerland, 2021; pp. 901–933. ISBN 978-3-030-52171-4.
3. Molod, A.; Salmun, H.; Dempsey, M. Estimating Planetary Boundary Layer Heights from NOAA Profiler Network Wind Profiler Data. *J. Atmos. Ocean. Technol.* **2015**, *32*, 1545–1561. [CrossRef]
4. Nash, J.; Oakley, T.J. Development of COST 76 Wind Profiler Network in Europe. *Phys. Chem. Earth Part B Hydrol. Ocean. Atmos.* **2001**, *26*, 193–199. [CrossRef]
5. Ishihara, M.; Kato, Y.; Abo, T.; Kobayashi, K.; Izumikawa, Y. Characteristics and Performance of the Operational Wind Profiler Network of the Japan Meteorological Agency. *J. Meteorol. Soc. Jpn. Ser. II* **2006**, *84*, 1085–1096. [CrossRef]
6. Kim, K.-H.; Kim, M.-S.; Seo, S.-W.; Kim, P.-S.; Kang, D.-H.; Kwon, B.H. Quality Evaluation of Wind Vectors from UHF Wind Profiler Using Radiosonde Measurements. *J. Environ. Sci. Int.* **2015**, *24*, 133–150. [CrossRef]
7. Liu, B.; Guo, J.; Gong, W.; Shi, L.; Zhang, Y.; Ma, Y. Characteristics and Performance of Wind Profiles as Observed by the Radar Wind Profiler Network of China. *Atmos. Meas. Tech.* **2020**, *13*, 4589–4600. [CrossRef]
8. Gonzalez, S.; Bech, J.; Udina, M.; Codina, B.; Paci, A.; Trapero, L. Decoupling between Precipitation Processes and Mountain Wave Induced Circulations Observed with a Vertically Pointing K-Band Doppler Radar. *Remote Sens.* **2019**, *11*, 1034. [CrossRef]
9. Zhang, Y.; Guo, J.; Yang, Y.; Wang, Y.; Yim, S. Vertical Wind Shear Modulates Particulate Matter Pollutions: A Perspective from Radar Wind Profiler Observations in Beijing, China. *Remote Sens.* **2020**, *12*, 546. [CrossRef]
10. Garcia-Benadi, A.; Bech, J.; Gonzalez, S.; Udina, M.; Codina, B.; Georgis, J.F. Precipitation Type Classification of Micro Rain Radar Data Using an Improved Doppler Spectral Processing Methodology. *Remote Sens.* **2020**, *12*, 4113. [CrossRef]
11. Wang, D.; Giangrande, S.E.; Feng, Z.; Hardin, J.C.; Prein, A.F. Updraft and Downdraft Core Size and Intensity as Revealed by Radar Wind Profilers: MCS Observations and Idealized Model Comparisons. *J. Geophys. Res. Atmos.* **2020**, *125*, e2019JD031774. [CrossRef]
12. Politovich, M.K.; Goodrich, R.K.; Morse, C.S.; Yates, A.; Barron, R.; Cohn, S.A. The Juneau Terrain-Induced Turbulence Alert System. *Bull. Am. Meteorol. Soc.* **2011**, *92*, 299–313. [CrossRef]
13. Udina, M.; Bech, J.; Gonzalez, S.; Soler, M.R.; Paci, A.; Miró, J.R.; Trapero, L.; Donier, J.M.; Douffet, T.; Codina, B.; et al. Multi-Sensor Observations of an Elevated Rotor during a Mountain Wave Event in the Eastern Pyrenees. *Atmos. Res.* **2020**, *234*, 104698. [CrossRef]
14. Wang, C.; Chen, M.; Chen, Y. Impact of Combined Assimilation of Wind Profiler and Doppler Radar Data on a Convective-Scale Cycling Forecasting System. *Mon. Weather Rev.* **2022**, *150*, 431–450. [CrossRef]
15. Degelia, S.K.; Wang, X.; Stensrud, D.J.; Turner, D.D. Systematic Evaluation of the Impact of Assimilating a Network of Ground-Based Remote Sensing Profilers for Forecasts of Nocturnal Convection Initiation during PECAN. *Mon. Weather Rev.* **2020**, *148*, 4703–4728. [CrossRef]
16. Schraff, C.; Reich, H.; Rhodin, A.; Schomburg, A.; Stephan, K.; Periáñez, A.; Potthast, R. Kilometre-scale Ensemble Data Assimilation for the COSMO Model (KENDA). *Q. J. R. Meteorol. Soc.* **2016**, *142*, 1453–1472. [CrossRef]
17. Liu, D.; Huang, C.; Feng, J. Influence of Assimilating Wind Profiling Radar Observations in Distinct Dynamic Instability Regions on the Analysis and Forecast of an Extreme Rainstorm Event in Southern China. *Remote Sens.* **2022**, *14*, 3478. [CrossRef]
18. Ralph, F.M.; Neiman, P.J.; Ruffieux, D. Precipitation Identification from Radar Wind Profiler Spectral Moment Data: Vertical Velocity Histograms, Velocity Variance, and Signal Power–Vertical Velocity Correlations. *J. Atmos. Ocean. Technol.* **1996**, *13*, 545–559. [CrossRef]
19. Radenz, M.; Bühl, J.; Lehmann, V.; Görsdorf, U.; Leinweber, R. Combining Cloud Radar and Radar Wind Profiler for a Value Added Estimate of Vertical Air Motion and Particle Terminal Velocity within Clouds. *Atmos. Meas. Tech.* **2018**, *11*, 5925–5940. [CrossRef]

20. Tsai, S.-C.; Chu, Y.-H.; Chen, J.-S. Identification of Concurrent Clear-Air and Precipitation Doppler Profiles for VHF Radar and an Incorporating Study of Strongly Convective Precipitation with Dual-Polarized Microwave Radiometer. *Atmosphere* **2022**, *13*, 557. [CrossRef]
21. Lundquist, J.D.; Neiman, P.J.; Martner, B.; White, A.B.; Gottas, D.J.; Ralph, F.M. Rain versus Snow in the Sierra Nevada, California: Comparing Doppler Profiling Radar and Surface Observations of Melting Level. *J. Hydrometeorol.* **2008**, *9*, 194–211. [CrossRef]
22. Valdivia, J.M.; Scipión, D.E.; Milla, M.; Silva, Y. Multi-Instrument Rainfall-Rate Estimation in the Peruvian Central Andes. *J. Atmos. Ocean. Technol.* **2020**, *37*, 1811–1826. [CrossRef]
23. Ryzhkov, A.V.; Schuur, T.J.; Burgess, D.W.; Heinselman, P.L.; Giangrande, S.E.; Zrnic, D.S. The Joint Polarization Experiment: Polarimetric Rainfall Measurements and Hydrometeor Classification. *Bull. Am. Meteorol. Soc.* **2005**, *86*, 809–824. [CrossRef]
24. Besic, N.; Ventura, J.F.I.; Grazioli, J.; Gabella, M.; Germann, U.; Berne, A. Hydrometeor Classification through Statistical Clustering of Polarimetric Radar Measurements: A Semi-Supervised Approach. *Atmos. Meas. Tech.* **2016**, *9*, 4425–4445. [CrossRef]
25. Chen, Y.; Liu, X.; Bi, K.; Zhao, D. Hydrometeor Classification of Winter Precipitation in Northern China Based on Multi-Platform Radar Observation System. *Remote Sens.* **2021**, *13*, 5070. [CrossRef]
26. González, S.; Bech, J.; Garcia-Benadí, A.; Udina, M.; Codina, B.; Trapero, L.; Paci, A.; Georgis, J.-F. Vertical Structure and Microphysical Observations of Winter Precipitation in an Inner Valley during the Cerdanya-2017 Field Campaign. *Atmos. Res.* **2021**, *264*, 105826. [CrossRef]
27. O'Hora, F.; Bech, J. Improving Weather Radar Observations Using Pulse-Compression Techniques. *Meteorol. Appl.* **2007**, *14*, 389–401. [CrossRef]
28. Campistron, B.; Réchou, A. Rain Kinetic Energy Measurement with a UHF Wind Profiler: Application to Soil Erosion Survey of a Volcanic Tropical Island. In Proceedings of the 13th International Workshop on Technical and Scientific Aspects of MST Radars, Kühlungsborn, Germany, 19–23 March 2012; pp. 47–51. Available online: https://www.iap-kborn.de/MST13/files/mst13proceedings.pdf (accessed on 8 August 2022).
29. Peters, G.; Fischer, B.; Andersson, T. Rain Observations with a Vertically Looking Micro Rain Radar (MRR). *Boreal Environ. Res.* **2002**, *7*, 353–362.
30. Chang, W.Y.; Lee, G.W.; Jou, B.J.D.; Lee, W.C.; Lin, P.L.; Yu, C.K. Uncertainty in Measured Raindrop Size Distributions from Four Types of Collocated Instruments. *Remote Sens.* **2020**, *12*, 1167. [CrossRef]
31. Tokay, A.; Wolff, D.B.; Petersen, W.A. Evaluation of the New Version of the Laser-Optical Disdrometer, OTT Parsivel2. *J. Atmos. Ocean. Technol.* **2014**, *31*, 1276–1288. [CrossRef]
32. World Meteorological Organization. *Manual on Codes—International Codes, Volume I.1, Annex II to the WMO Technical Regulations: Part A—Alphanumeric Codes*; World Meteorological Organization: Geneva, Switzerland, 2019; ISBN 978-92-63-10306-2.
33. Koistinen, J.; Saltikoff, E. Experience of Customer Products of Accumulated Snow, Sleet and Rain. *COST75 Adv. Weather Radar Syst.* **1998**, *397*, 406.
34. Casellas, E.; Bech, J.; Veciana, R.; Pineda, N.; Miró, J.R.; Moré, J.; Rigo, T.; Sairouni, A. Nowcasting the Precipitation Phase Combining Weather Radar Data, Surface Observations, and NWP Model Forecasts. *Q. J. R. Meteorol. Soc.* **2021**, *147*, 3135–3153. [CrossRef]
35. Casellas, E.; Bech, J.; Veciana, R.; Pineda, N.; Rigo, T.; Miró, J.R.; Sairouni, A. Surface Precipitation Phase Discrimination in Complex Terrain. *J. Hydrol.* **2021**, *592*, 125780. [CrossRef]
36. Anandan, V.K.; Balamuralidhar, P.; Rao, P.B.; Jain, A.R.; Pan, C.J. An Adaptive Moments Estimation Technique Applied to MST Radar Echoes. *J. Atmos. Ocean. Technol.* **2005**, *22*, 396–408. [CrossRef]
37. Allabakash, S.; Yasodha, P.; Bianco, L.; Reddy, S.V.; Srinivasulu, P. Improved Moments Estimation for VHF Active Phased Array Radar Using Fuzzy Logic Method. *J. Atmos. Ocean. Technol.* **2015**, *32*, 1004–1014. [CrossRef]
38. Price-Whelan, A.M.; Sipőcz, B.M.; Günther, H.M.; Lim, P.L.; Crawford, S.M.; Conseil, S.; Shupe, D.L.; Craig, M.W.; Dencheva, N.; Ginsburg, A.; et al. The Astropy Project: Building an Open-Science Project and Status of the v2.0 Core Package. *Astron. J.* **2018**, *156*, 123. [CrossRef]
39. Atlas, D.; Srivastava, R.C.; Sekhon, R.S. Doppler Radar Characteristics of Precipitation at Vertical Incidence. *Rev. Geophys.* **1973**, *11*, 1–35. [CrossRef]
40. Ralph, F.M.; Neiman, P.J.; van de Kamp, D.W.; Law, D.C. Using Spectral Moment Data from NOAA's 404-MHz Radar Wind Profilers to Observe Precipitation. *Bull. Am. Meteorol. Soc.* **1995**, *76*, 1717–1739. [CrossRef]
41. Ulbrich, C.W. Natural Variations in the Analytical Form of the Raindrop Size Distribution. *J. Clim. Appl. Meteorol.* **1983**, *22*, 1764–1775. [CrossRef]
42. Chu, Y.-H.; Su, C.-L. An Investigation of the Slope–Shape Relation for Gamma Raindrop Size Distribution. *J. Appl. Meteorol. Climatol.* **2008**, *47*, 2531–2544. [CrossRef]
43. Gunn, R.; Kinzer, G.D. The Terminal Velocity of Fall for Water Droplets in Stagnant Air. *J. Meteorol.* **1949**, *6*, 243–248. [CrossRef]
44. Cerro, C.; Bech, J.; Codina, B.; Lorente, J. Modeling Rain Erosivity Using Disdrometric Techniques. *Soil Sci. Soc. Am. J.* **1998**, *62*, 731–735. [CrossRef]
45. Jolliffe, I.T.; Stephenson, D.B. *Forecast Verification: A Practitioner's Guide in Atmospheric Science*; John Wiley & Sons: Hoboken, NJ, USA, 2012; ISBN 978-1-119-96000-3.